Infrared Spectroscopy of Propene in Solid para-Hydrogen and Helium Droplets: the Role of Matrix Shifts in the Analysis of Anharmonic Resonances

Gregory T. Pullen[a], Peter R. Franke[a], Yuan-Pern Lee[b,c,d], and Gary E. Douberly[a]*

[a] Department of Chemistry, University of Georgia, Athens, GA 30602, USA

[b] Department of Applied Chemistry and Institute of Molecular Science, National Chiao Tung University, Hsinchu 30010, Taiwan

[c] Center for Emergent Functional Matter Science, National Chiao Tung University, Hsinchu 30010, Taiwan

[d] Institute of Atomic and Molecular Sciences, Academia Sinica, Taipei 10617, Taiwan

* Corresponding Author: Email: douberly@uga.edu Tele: 01-706-542-3857

Abstract

The infrared spectrum of propene in the CH stretching region is complicated by anharmonic resonance polyads associated with the coupling of CH stretch fundamentals to overtones and combinations of CH_n bends and CC stretches. We report the spectra of propene isolated in both helium nanodroplets (HENDI) and solid *para*-hydrogen (*p*-H_2). Spectral assignments and anharmonic polyad memberships are obtained with a VPT2+K effective Hamiltonian. In the 2800 to 3120 cm^{-1} region, the average differential matrix shift in going from HENDI to *p*-H_2 is ~4.4 cm^{-1} to the red, with a standard deviation of 1.9 cm^{-1}. Moreover, the choice of matrix environment influences the positions and intensity ratios of transitions within the resonance polyads. Two-state interaction models are used to confirm that differential matrix shifts less than 10 cm^{-1} are sufficient to account for the observed differences.

Keywords

para-Hydrogen matrix isolation, Helium nanodroplet isolation, Propene infrared spectroscopy, Anharmonic resonance polyads, Effective Hamiltonian calculations

1. Introduction

Vibrational spectra recorded using matrix isolation techniques exhibit shifts due to the perturbative effects of the host environment [1, 2]. The extent to which a band is shifted depends on the strength and anisotropy of the guest-host interaction, which is known to be vibrational mode-specific. In comparison to solid-argon, solid-neon exhibits weaker guest-host interactions, and infrared (IR) spectra obtained using solid-neon typically exhibit comparatively smaller band origin shifts and reduced inhomogeneous broadening effects [3, 4]. It is generally accepted that solid *para*-hydrogen (*p*-H_2) [5-14] and helium nanodroplet (HENDI) [15-22] isolation techniques are even better than solid-Ne in regard to reducing matrix-induced broadening effects, owing to the quantum nature of the host environments; and in the case of helium droplets, band origins are typically shifted by less than 1 cm^{-1}. While comparisons between *p*-H_2 and HENDI are somewhat limited [23-31], band origins in *p*-H_2 spectra are typically 3-10 cm^{-1} to the red of those in HENDI spectra. In the present work, we carry out an extensive comparison of the IR spectra of propene measured with either *p*-H_2 or HENDI.

Propene has been studied with microwave [32-35], photoelectron [36] and IR spectroscopy [37-48], along with various theoretical methods [49-52]. IR spectra in the 3 μm region were recorded at temperatures greater than 300 K, to obtain temperature dependent absorption cross-sections [46, 47]. It was noted that the spectra in this temperature regime are difficult to assign and are complicated by the presence of many overlapping bands, all of which exhibit extensive rotational fine structure. Above 2800 cm^{-1}, intense Q-branch features have been assigned to the six CH stretch fundamentals and the overtone of the γ-CH_3 antisymmetric bend. However, upon cooling propene to less than 0.4 K in liquid helium droplets, the spectrum between 2800 and 3120 cm^{-1} contains 26 resolved vibrational bands. The extensive anharmonic coupling associated with this frequency region is analyzed with a second order vibrational perturbation theory plus resonances (VPT2+K) effective Hamiltonian approach [53], leading to several new assignments in the 3 μm region. Moreover, an analysis of the differential matrix shifts associated with the *p*-H_2 and HENDI host environments is carried out, revealing an average 4.4 cm^{-1} red shift over this frequency region. As a result of the anharmonic resonance polyads, small differential perturbations by the matrix host environments manifest as large

changes in the relative intensities of bands in the spectrum, as bright/dark states are tuned either into or out of resonance.

2. Methods

2.1. HENDI Experiment

The instrument used to measure HENDI spectra has previously been described in detail [18-20, 54]; a brief description is given for the details relevant to the propene measurements. Helium gas at a backing pressure of ~35 bar passes into the vacuum chamber through a ~17 K cryogenic nozzle with a ~5 μm orifice diameter, leading to supersonic expansion and subsequent homogeneous nucleation of droplets consisting on average of several thousand atoms. Droplets evaporatively cool to ~0.4 K. The droplets are collimated into a beam by a 0.4 mm conical skimmer before entering a differentially pumped pick-up chamber. Inside the pick-up chamber, the droplet beam passes through a ~3.5 cm long pick-up cell where propene is doped into the droplets. Propene is maintained at a pressure of ~2 x 10^{-6} Torr within the pick-up cell as measured by an ion gauge calibrated for N_2. This was determined to be a factor of 2-3 less than optimal for pick-up of a single propene molecule. These conditions were chosen to significantly reduce the probability for the sequential capture of two propene molecules by a single helium droplet.

The mid-IR idler output from a continuous wave optical parametric oscillator (cw-OPO) counter-propagates the droplet beam. The tuning and calibration of the cw-OPO have previously been described [55]. When propene is vibrationally excited, He atoms are evaporated from the droplet to dissipate the absorbed energy. The loss of He atoms induces a reduction in the geometric and ionization cross-sections of the droplets, and the ionization cross-section reduction is measured with a quadrupole mass spectrometer (QMS). The droplets are ionized *via* electron impact ionization by an axial-beam ionizer within the QMS. The propene molecule then becomes ionized *via* He^+ charge transfer; the ionization mechanism has been previously described [19, 56, 57]. Ionization and fragmentation of propene leads to a large ion signal at m/z = 39 u ($C_3H_3^+$), which can be used to discriminate against other impurities and achieve quasi-species-selective IR spectra. The cw-OPO is amplitude modulated at ~80 Hz and the ion signal

is measured on a lock-in amplifier, leading to low background photon-induced depletion signals of the neutral dopant molecules within the superfluid helium nanodroplets as the IR radiation is tuned with ~20 MHz resolution. The IR spectra are normalized to the mid-IR idler power.

2.2. *p*-H_2 Matrix Isolation Experiment

The instrument used to measure spectra in solid *para*-hydrogen matrices has previously been described [58-60], so we will only briefly review the important details here. An ~3.3 K gold-coated copper plate serves as both a matrix sample substrate and a mirror to reflect the IR beam to the detector. A Fourier-transform infrared (FTIR) spectrometer (Bruker Vertex 80v) equipped with a KBr beam splitter and a HgCdTe detector held at ~77 K is used to record IR absorption spectra from 500 – 4000 cm^{-1}. For each spectrum collected, 200 scans are averaged at a spectrometer resolution of ~0.25 cm^{-1}.

The production of *p*-H_2 gas has been described previously [13]. *p*-H_2 is prepared by passing normal hydrogen gas (*n*-H_2: ~75% *o*-H_2 / ~25% *p*-H_2 at room temperature) through an iron(III)-oxide catalyst cooled to ~12.9 K, leading to an estimated final concentration of *o*-H_2 at less than 100 ppm. Propene (≥99.5%, AGA Specialty Gases) is mixed with *p*-H_2, and the gaseous mixture of propene/*p*-H_2 (~1/1700) is deposited over ~10 hours at a flow rate of 10 – 13 mmol/hr. At a concentration of ~600 ppm, the average distance between embedded propene molecules is ~4 nm, which makes dimer formation unlikely. Moreover, intermolecular interactions between adjacent propene molecules do not affect the recorded spectra.

2.3.VPT2+K Calculations

The theoretical methods used here have been described in detail [53, 61, 62]. All electronic structure calculations were carried out using the CFOUR software package [63]. Core electrons were kept frozen during the correlation treatment. Propene was optimized to the C_s symmetry electronic global minimum structure and then a semi-diagonal quartic force field was computed, all at the CCSD(T)/ANO1 level of theory [64-70]. In addition, propene was optimized and harmonic frequencies were computed at the CCSD(T)/ANO2 level of theory. The CCSD(T)/ANO2 quadratic force constants and linear dipole derivatives were used in lieu of their CCSD(T)/ANO1 counterparts. This hybrid force field was used as input into our second-order vibrational perturbation theory with resonances (VPT2+K) code [71-74].

VPT2+K is implemented using an in-house script written in *Mathematica 10* [75]; it consists of a full VPT2 treatment, followed by deperturbation of strong interactions as determined by energy comparisons of states and the Martin test [53, 76]. These strong interactions are then treated explicitly *via* diagonalization of an effective Hamiltonian that accounts for both Fermi and Darling-Dennison type resonances. The effective Hamiltonian for propene contains 61 vibrational states. The entire effective Hamiltonian is given in Table S1 of the Supporting Information. Electrical harmonicity is assumed, *i.e.* the harmonic intensities of the bright CH stretch fundamentals are distributed into the dark states proportional to the squares of their eigenvector coefficients.

3. Results

The spectra of propene from 2800 to 3120 cm^{-1} are shown in Fig. 1. The harmonic frequency simulation calculated at the CCSD(T)/ANO2 level of theory and scaled by 0.955 is shown in Fig. 1(a), with the harmonic modes, frequencies, and intensities given in Table 1. A deperturbed VPT2 simulation calculated at the CCSD(T)/ANO1 level of theory is shown in Fig. 1(b), with the DVPT2 frequencies and intensities given in Table S2 of the Supporting Information. The VPT2+K simulation calculated using the CCSD(T)/ANO2//CCSD(T)/ANO1 hybrid force field is shown in Fig. 1(c), with the VPT2+K frequencies, intensities, and compositions given in Table 2. The HENDI spectrum is shown in Fig. 1(d), and the *p*-H_2 spectrum is shown in Fig. 1(e). The band origins, intensities, and relative line shifts between the HENDI and *p*-H_2 spectra in the region of 2800 – 3120 cm^{-1} are given in Table 3, with the gas-phase band origins given where possible for comparison. The entire *p*-H_2 spectrum from 500 – 4000 cm^{-1} is shown in Figs. S1 and S2 of the Supporting Information. Assignments for the entire *p*-H_2 and HENDI spectra, with comparisons to previous literature, are given in Table S3 of the Supporting Information. We focus the following discussion on a comparison of spectra measured in the CH stretching region, but we note here that a previously unassigned ν_{16} / $\nu_{14}+\nu_{17}$ Fermi dyad was found in the *p*-H_2 spectra at 1440.1 / 1472.5 cm^{-1}. All other bands observed below 2800 cm^{-1} have been previously assigned in the gas phase (see Table S3).

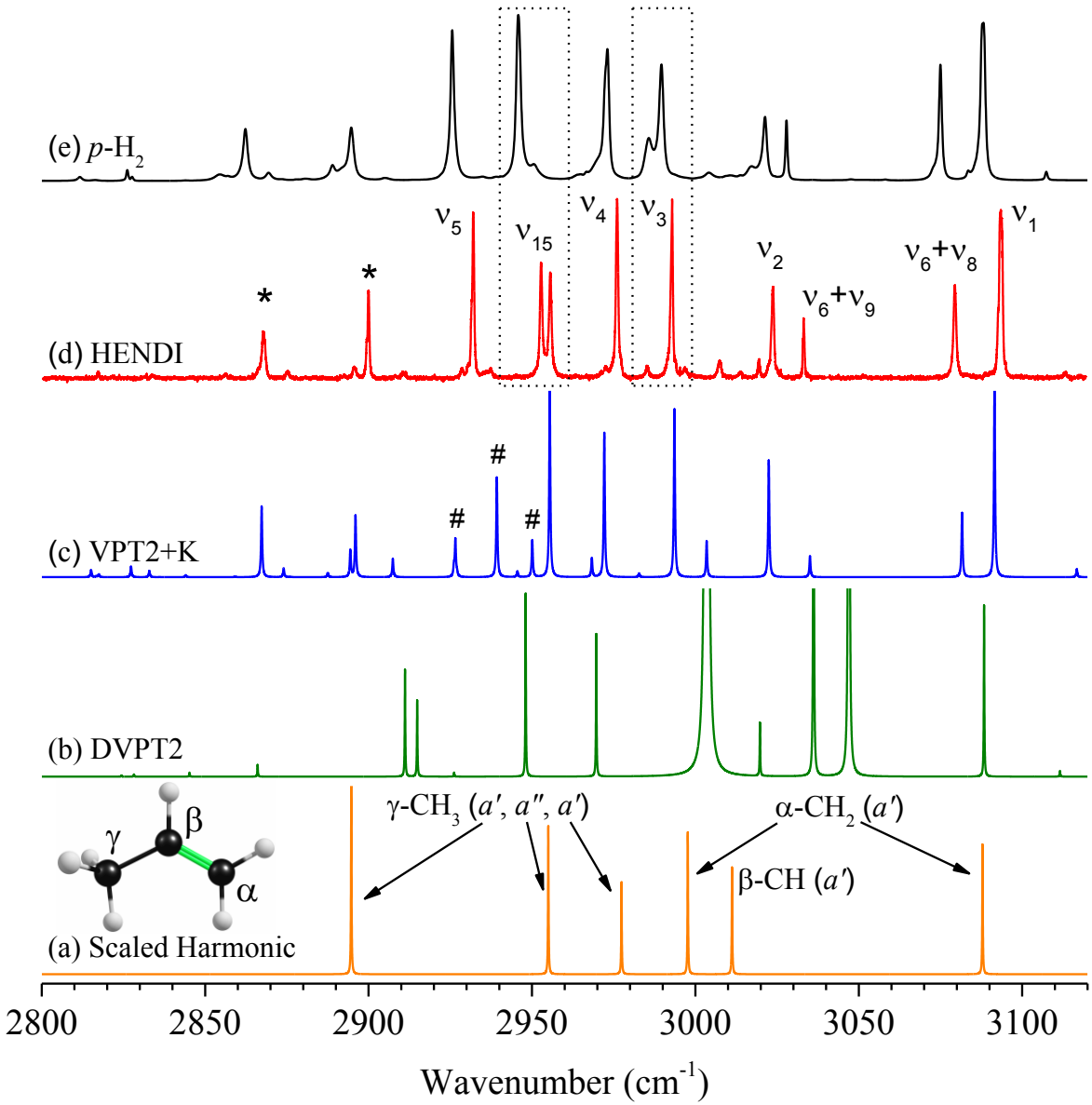

Fig. 1. Comparison of experimental spectra with simulations for propene in the region from 2800 – 3120 cm^{-1}. (a) Harmonic frequency simulation scaled by 0.955. (b) Deperturbed VPT2 simulation. (c) VPT2+K simulation. (d) HENDI spectrum. (e) *p*-H_2 spectrum. Assignments of the more intense bands observed in the HENDI spectrum are based on the eigenvector components from the VPT2+K effective Hamiltonian results (see Table 2 for detailed description of anharmonic polyad memberships). The pair of bands marked as ν_{15} are members of an anharmonic polyad, but the largest mixing likely occurs between ν_{15} and $\nu_7+\nu_{12}+\nu_{20}$. The bands marked by asterisks are heavily mixed modes whose intensities derive from either ν_5 or ν_{15}. The bands marked by # are mixed modes whose intensities derive from ν_5; the intensity borrowing in this region is over predicted by VPT2+K (see text).

Table 1. The harmonic modes of propene and their frequencies (cm^{-1}) and intensities (km/mol) at the CCSD(T)/ANO1 and CCSD(T)/ANO2 levels of theory.

		ANO1		ANO2		
		Freq	Int	Freq	Int	Mode Type [a]
ν_1	a'	3234.0	14.4	3233.4	13.0	α-CH_2 antisymmetric C-H stretch
ν_2	a'	3155.8	11.5	3153.1	10.7	β-CH C-H stretch
ν_3	a'	3141.6	13.6	3138.9	14.2	α-CH_2 symmetric C-H stretch
ν_4	a'	3117.3	11.0	3117.7	9.2	γ-CH_3 antisymmetric C-H stretch
ν_5	a'	3030.8	19.6	3031.1	19.1	γ-CH_3 symmetric C-H stretch
ν_6	a'	1695.0	9.5	1696.6	10.7	α-β C=C stretch
ν_7	a'	1498.0	12.8	1501.0	13.2	γ-CH_3 antisymmetric C-H bend
ν_8	a'	1451.8	1.2	1454.2	1.2	α-CH_2 C-H bend
ν_9	a'	1406.1	1.5	1408.9	1.5	γ-CH_3 symmetric C-H bend
ν_{10}	a'	1320.5	0.2	1322.1	0.1	β-CH C-H bend
ν_{11}	a'	1191.5	0.2	1194.0	0.1	in-phase α-CH_2 + γ-CH_3 rock
ν_{12}	a'	941.5	3.2	942.8	3.1	out-of-phase α-CH_2 + γ-CH_3 rock
ν_{13}	a'	929.4	1.9	932.1	2.0	β-γ C-C stretch
ν_{14}	a'	419.2	0.9	420.3	0.9	C-C-C bend
ν_{15}	a''	3093.6	16.8	3094.2	14.9	γ-CH_3 antisymmetric C-H stretch
ν_{16}	a''	1484.6	6.3	1487.8	6.3	γ-CH_3 antisymmetric C-H bend
ν_{17}	a''	1067.4	2.6	1068.8	2.6	γ-CH_3 rock
ν_{18}	a''	1018.6	13.0	1018.0	12.6	β-CH H wag
ν_{19}	a''	929.7	38.8	929.5	38.3	α-CH_2 C-H wag
ν_{20}	a''	583.3	11.0	583.7	11.0	β-CH C wag
ν_{21}	a''	201.9	0.4	203.8	0.4	γ-CH_3 methyl torsion

[a] Refer to Figure 1 for definition of α, β, and γ.

Table 2. VPT2+K frequencies (cm^{-1}), intensities (km/mol), and percent compositions (squared eigenvector coefficients x 100) in the region 2800 – 3120 cm^{-1}. Dark state components are typically shown only if they contribute greater than 10 percent to an eigenvector (see Table S4 for more extensive version of this table). Bands that have been confidently assigned in the experimental spectrum are marked with bold type. The largest contributing eigenvector components (which inform the assignments given in Fig. 1) are also shown in bold.

Freq	Int	Percent Composition
2815.09	0.40	3% ν_{15} + 81% $\nu_9+\nu_{16}$ + 12% $\nu_9+\nu_{14}+\nu_{17}$
2817.46	0.16	1% ν_1 + 84% $\nu_6+\nu_{11}$ + 11% $\nu_7+\nu_{12}+\nu_{14}$
2827.32	0.60	2% ν_2 + 2% ν_3 + 82% $2\nu_8$
2832.92	0.34	2% ν_4 + 1% ν_5 + 86% $\nu_7+\nu_9$
2844.07	0.11	1% ν_{15} + 11% $\nu_9+\nu_{16}$ + 82% $\nu_9+\nu_{14}+\nu_{17}$
2867.28	**3.95**	**21% ν_5** + **19% $\nu_7+\nu_8$** + **35% $2\nu_{16}$**
2874.02	0.49	1% ν_3 + 3% ν_4 + 63% $\nu_7+\nu_8$ + 19% $2\nu_{16}$
2887.49	0.19	1% ν_{15} + 54% $\nu_8+\nu_{14}+\nu_{17}$ + 27% $\nu_9+\nu_{12}+\nu_{20}$
2894.41	1.49	10% ν_{15} + 72% $\nu_7+\nu_{16}$
2896.00	**3.42**	**18% ν_5 + 19% $2\nu_7$** + **40% $\nu_{14}+\nu_{16}+\nu_{17}$** + 11% $2\nu_{14}+2\nu_{17}$
2907.42	1.02	3% ν_4 + 4% ν_5 + 28% $2\nu_7$ + 22% $2\nu_{16}$ + 23% $\nu_{14}+\nu_{16}+\nu_{17}$ + 13% $2\nu_{14}+2\nu_{17}$
2926.11	0.54	4% ν_{15} + 68% $\nu_7+\nu_{14}+\nu_{17}$ + 21% $\nu_8+\nu_{12}+\nu_{20}$
2926.56	2.05	1% ν_1 + 13% ν_2 + 2% ν_3 + 3% ν_4 + 77% $\nu_6+\nu_{10}$
2927.06	0.19	1% ν_{15} + 20% $\nu_7+\nu_{14}+\nu_{17}$ + 71% $\nu_8+\nu_{12}+\nu_{20}$
2939.24	**5.55**	**29% ν_5** + **35% $2\nu_7$** + **16% $\nu_{12}+\nu_{16}+\nu_{20}$** + 10% $2\nu_{14}+2\nu_{17}$
2945.54	0.33	2% ν_5 + 10% $\nu_{12}+\nu_{16}+\nu_{20}$ + 22% $\nu_{14}+\nu_{16}+\nu_{17}$ + 63% $2\nu_{14}+2\nu_{17}$
2950.09	2.06	2% ν_4 + 10% ν_5 + 10% $2\nu_{16}$ + 56% $\nu_{12}+\nu_{16}+\nu_{20}$
2955.44	**10.59**	**71% ν_{15}** + 12% $\nu_7+\nu_{16}$ + 12% $\nu_7+\nu_{12}+\nu_{20}$
2968.32	**1.06**	7% ν_{15} + **82% $\nu_7+\nu_{12}+\nu_{20}$**
2972.13	**8.03**	1% ν_2 + 16% ν_3 + **60% ν_4** + 4% $\nu_6+\nu_8$ + 4% $\nu_6+\nu_{10}$ + 4% $2\nu_{16}$
2982.78	**0.21**	1% ν_3 + **85% $\nu_{12}+\nu_{14}+\nu_{17}+\nu_{20}$**
2993.59	**9.34**	**52% ν_3** + 21% ν_4 + 7% $\nu_6+\nu_8$ + 8% $\nu_6+\nu_9$
3003.45	**2.01**	12% ν_2 + 5% ν_3 + **79% $\nu_6+\nu_{12}+\nu_{14}$**
3022.46	**6.50**	**61% ν_2** + 17% $\nu_6+\nu_{10}$ + 12% $\nu_6+\nu_{12}+\nu_{14}$
3035.06	**1.18**	2% ν_2 + 6% ν_3 + 1% ν_4 + **88% $\nu_6+\nu_9$**
3081.60	**3.58**	15% ν_1 + 4% ν_2 + 9% ν_3 + **67% $\nu_6+\nu_8$**
3091.53	**10.87**	**81% ν_1** + 1% ν_2 + 2% ν_3 + 11% $\nu_6+\nu_8$
3116.72	**0.44**	3% ν_3 + **93% $\nu_6+\nu_7$**

Table 3. Comparison of observed band origins (cm^{-1}), intensities (a.u.), and differential matrix shifts (cm^{-1}) in going from HENDI to *p*-H_2. Gas phase values are from Refs. [37, 38, 46, 47] and should be viewed as approximate owing to the nature of the high-temperature measurement. Assignments are based on the eigenvector components from the VPT2+K effective Hamiltonian analysis. The asterisks indicate modes that are heavily mixed; see Tables 2 and S4 for a detailed description of anharmonic polyad components. Intensities are given as a percentage of the most intense band in each spectrum.

***p*-H_2**		**HENDI**		**Red Shift**	**Gas**	**Assignment**	**VPT2+K**
Freq	Int	Freq	Int	Freq	Freq		Freq
2811.65	2.2	2817.28	1.8	5.63			
2816.33	0.5	2821.66	0.4	5.33			
2826.17	2.8	2831.6	0.6	5.43			
2827.66	0.8	2833.89	1.4	6.23			
2855	8.6	2856.25	2.1	1.25			
2862.31	32.9	2867.8	30.2	5.49	2868.2	$2\nu_{16}$ *	2867.3
2869.44	6.1	2875.23	3.2	5.79			
2888.97	8.6	2895.68	7.2	6.71			
2894.7	44.7	2899.96	31.0	5.26		$\nu_{14}+\nu_{16}+\nu_{17}$ *	2896.0
2905.17	2.2	2910.0	3.7	4.83			
2925.61	77.3	2932.0	65.5	6.39	2931.5	ν_5	2939.2
2934.84	2.8	2937.0	8.4	2.16			
2945.87	100	2952.8	53.1	6.93	2954.3	ν_{15} / $\nu_7+\nu_{12}+\nu_{20}$	2955.4
2950.66	15.1	2955.6	52.0	4.94		ν_{15} / $\nu_7+\nu_{12}+\nu_{20}$	2968.3
2965.5	6.0	2972.4	7.9	6.9			
2972.8	90.4	2976.0	75.7	3.2	2973.0	ν_4	2972.1
2985.74	36.6	2985.26	6.0	-0.48		ν_3/ $\nu_{12}+\nu_{14}+\nu_{17}+\nu_{20}$	2982.8
2989.61	65.9	2992.8	74.9	3.19	2991.0	ν_3/ $\nu_{12}+\nu_{14}+\nu_{17}+\nu_{20}$	2993.6
2995.1	2.5	2997.0	7.8	1.9			
3004.15	8.9	3007.41	11.1	3.26		$\nu_6+\nu_{12}+\nu_{14}$	3003.5
3011	5.3	3013.77	3.8	2.77			
3017.44	18.5	3019.42	5.8	1.98			
3021.3	33.9	3023.7	44.2	2.4	3012.8	ν_2	3022.5
3027.87	15.3	3033.14	16.4	5.27		$\nu_6+\nu_9$	3035.1
3074.97	50.8	3079.4	51.4	4.43		$\nu_6+\nu_8$	3081.6
3087.98	96.9	3093.45	100	5.47	3091.6	ν_1	3091.5
3107.37	3.3	3113.2	3.3	5.83		$\nu_6+\nu_7$	3116.7

Comparing the HENDI propene spectra to gas-phase assignments reported in the literature, we find an average matrix red shift of 1.7 ± 0.8 cm^{-1}. We note that the HENDI matrix shift for ν_2 (11 cm^{-1} to the blue) is an outlier, and is not included in the above average. The discrepancy here is likely due to a problem with the reported gas-phase band origin, which is derived from low-resolution room temperature data [37]. Comparing the HENDI and *p*-H_2 spectra, we find that the spectra are qualitatively similar, with the bands in the *p*-H_2 spectrum typically red-shifted from those in the HENDI spectrum. It is also interesting to note that the bands in the *p*-H_2 spectra are broader on average, likely owing to an inhomogeneous effect associated with the non-crystalline nature of the *p*-H_2 matrix. On average, there is a 4.4 ± 1.9 cm^{-1} red shift observed when going from HENDI to *p*-H_2. The rather large standard deviation suggests the possibility for pairs of peaks shifting closer together or further apart in one matrix environment relative to the other, which can induce either a tuning or detuning of anharmonic resonances, as described below. We observe this behavior in two spectral regions, *i.e.* between 2940 – 2960 cm^{-1} and 2980 – 3000 cm^{-1} (marked by dashed boxes in Fig 1).

In the lower region from 2940 – 2960 cm^{-1}, the HENDI spectrum contains a pair of bands separated by ~2.8 cm^{-1} (2952.8 cm^{-1} / 2955.6 cm^{-1}) having a relative intensity ratio of ~51/49. This region of the *p*-H_2 spectrum also contains two bands, but they are separated by ~4.8 cm^{-1} (2945.9 cm^{-1} / 2950.7 cm^{-1}) and have a relative intensity ratio of ~87/13. This suggests that the lower of these two states correlates with a *bright* state (*i.e.* a CH stretch fundamental, in the detuning limit) and that the upper of these two states correlates with a *dark* state. Apparently, both states have a *differential* matrix shift to the *red*, with the lower (bright) state being shifted to a larger extent; and therefore, in going from He droplets to *p*-H_2, the resonance is detuned. From the VPT2+K analysis, and *via* the model described in detail below, the assignment of the bright/dark state interaction is determined to be largely an anharmonic resonance between ν_{15} and $\nu_7+\nu_{12}+\nu_{20}$. This is not expected to be a direct coupling; rather, the interaction derives from mutual coupling to a third state (*vide infra*).

Similarly in the upper region from 2980 – 3000 cm^{-1}, the HENDI spectrum contains a pair of bands separated by ~7.5 cm^{-1} (2985.3 cm^{-1} / 2992.8 cm^{-1}) having a relative intensity ratio of ~7/93. Again, this region of the *p*-H_2 spectrum contains two bands, but they are separated by ~3.9 cm^{-1} (2985.7 cm^{-1} / 2989.6 cm^{-1}) and have a relative intensity ratio of ~36/64. This suggests

that the upper of these two states correlates with a bright state, and the lower of these two states correlates with a dark state. In contrast to the 2940 – 2960 cm^{-1} region described above, the states in this region are tuned into resonance in going from He droplets to *p*-H_2.

4. Discussion

Assuming a two-state interaction between bright and dark states, 2×2 effective Hamiltonians can be derived for the regions of the HENDI and *p*-H_2 spectra between 2940 – 2960 cm^{-1} and 2980 – 3000 cm^{-1}, allowing for an approximate determination of the deperturbed state energies and off-diagonal coupling. The empirical eigenvector matrices (coefficients determined from the experimental band intensities) and the eigenvalue matrices (experimental band origins) can be used to calculate the initial effective Hamiltonians, as shown in Equation S1. The results of the effective Hamiltonians are shown in Table 4. In the lower region from 2940 – 2960 cm^{-1}, the lower, deperturbed (bright) state is red shifted by ~7.7 cm^{-1} in going from He droplets to *p*-H_2, and the upper (dark) state is red-shifted by ~4.2 cm^{-1}. Thus, while this pair of deperturbed states is nearly degenerate in He droplets, the mixing is made less extensive upon going to the *p*-H_2 matrix. In the upper region from 2980 – 3000 cm^{-1}, in going from He droplets to *p*-H_2, the lower (dark) state is blue shifted by ~1.3 cm^{-1} while the upper (bright) state is red-shifted by ~4.0 cm^{-1}. Thus, for this pair of states, the mixing is more extensive for *p*-H_2 matrix-isolated propene. From this rather simple analysis, it is evident that state-specific differential matrix shifts less than 10 cm^{-1} can lead to qualitative changes in the observed spectra, as a result of the tuning or detuning of anharmonic resonances. Moreover, the off-diagonal coupling is the same within about ±0.2 cm^{-1}, which is likely within the error of the model.

Table 4. Experimentally determined deperturbed states and off-diagonal coupling terms, assuming a two state interaction with a bright state and a dark state, as well as the shifts in going from HENDI to *p*-H_2.

	Lower (2940 – 2960 cm^{-1})			**Upper (2980 – 3000 cm^{-1})**		
	Bright	Dark	Coupling	Dark	Bright	Coupling
HENDI	2954.19	2954.21	1.40	2985.82	2992.24	1.98
p-H_2	2946.50	2950.03	1.62	2987.12	2988.23	1.85
Shift	-7.69	-4.18	0.22	1.30	-4.01	-0.13

The purely *ab initio* VPT2+K prediction of the propene spectrum is shown in Fig 1(c). The VPT2+K simulation matches the experimental spectra reasonably well, with the exception of the region around 2920 – 2950 cm^{-1}. The theoretical spectrum in this region overestimates the extent by which ν_5 is mixed with nearby dark states, with three moderately intense bands predicted (marked by # in Fig 1(c)), in contrast to the one intense band observed in either of the experimental spectra (2932 cm^{-1} in HENDI and 2926 cm^{-1} in *p*-H_2). We note that the DVPT2 theory shown in Fig 1(b) fails to qualitatively predict the experimental spectrum, which is due to the many strong resonances that are neglected with DVPT2 (see Table S2 for additional discussion).

To investigate the nature of the pairs of interacting states associated with the regions of the experimental spectra that differ qualitatively, we inspect the VPT2+K prediction in the vicinity of the boxed regions in Fig. 1. We can arrive at reasonable assignments, despite the fact that the predicted band positions are not particularly good in comparison to either the HENDI or *p*-H_2 spectra in these regions. We motivate assignments through the inspection of the eigenvector coefficients, which reveal the nature of the mixed states. For the lower frequency boxed region, the pairs of interacting states are assigned to ν_{15} (lower energy *bright* state) and $\nu_7+\nu_{12}+\nu_{20}$ (higher energy *dark* state). We note that the two eigenstates are rather extensive mixtures of basis states (see Table 2 and S4), and the assignments are based on the basis states with the largest squared eigenvector coefficients (VPT2+K prediction: 2955.4 cm^{-1}, 71% ν_{15}; 2968.3 cm^{-1}, 82% $\nu_7+\nu_{12}+\nu_{20}$). For the higher frequency boxed region, the assignments are $\nu_{12}+\nu_{14}+\nu_{17}+\nu_{20}$ (lower energy *dark* state) and ν_3 (higher energy *bright* state) (VPT2+K prediction: 2982.8 cm^{-1}, 85% $\nu_{12}+\nu_{14}+\nu_{17}+\nu_{20}$; 2993.6 cm^{-1}, 52% ν_3). Both of these interactions derive from coupling pathways involving at least one intermediary state (*vide infra*).

The spectra in the boxed regions are shown in greater detail in Fig. 2. Here the HENDI spectra are shown along the top of the figure (Fig 2(vi)), and the *p*-H_2 spectra are shown along the bottom (Fig 2(i)). The *ab initio* VPT2+K predictions are shown either directly above the *p*-H_2 spectrum (2940 – 2970 cm^{-1} region; left side of figure (Fig. 2a(ii))) or directly below the HENDI spectrum (2980 – 3000 cm^{-1} region; right side of figure (Fig. 2b(v))). Again, we emphasize that the band positions, for either matrix environment, are not predicted accurately in these regions, and we were guided by the relative intensities of the red and blue colored bands in choosing the

location of the *ab initio* VPT2+K spectra within Fig. 2. Notice that the *ab initio* prediction of the relative intensities for the bands assigned to (ν_{15} / $\nu_7+\nu_{12}+\nu_{20}$) match more closely the relative intensities in the *p*-H_2 spectrum, whereas the predicted intensities for the (ν_3 / $\nu_{12}+\nu_{14}+\nu_{17}+\nu_{20}$) bands match more closely those observed in the HENDI spectrum. For the 2980 – 3000 cm^{-1} region, red shifting the deperturbed ν_3 state within the 61 state Hamiltonian brings the intensity ratio into better agreement with that observed in the *p*-H_2 spectrum. Similarly, for the 2940 – 2960 cm^{-1} region, a red shift of the deperturbed $\nu_7+\nu_{12}+\nu_{20}$ state brings the simulated intensity ratio into better agreement with the HENDI spectrum. We emphasize here that the magnitudes and directions of the applied shifts are somewhat arbitrary (*e.g.* we could have applied a blue shift to $\nu_{12}+\nu_{14}+\nu_{17}+\nu_{20}$, rather than a red shift to ν_3), and the goal of the shifts is to simply show that the state assignments are reasonable, in the sense that the states are coupled and the resonances can be tuned *via* effective shifts on the order of 10 cm^{-1}. The intensity ratios and splitting results associated with this admittedly crude analysis are given in Table 5.

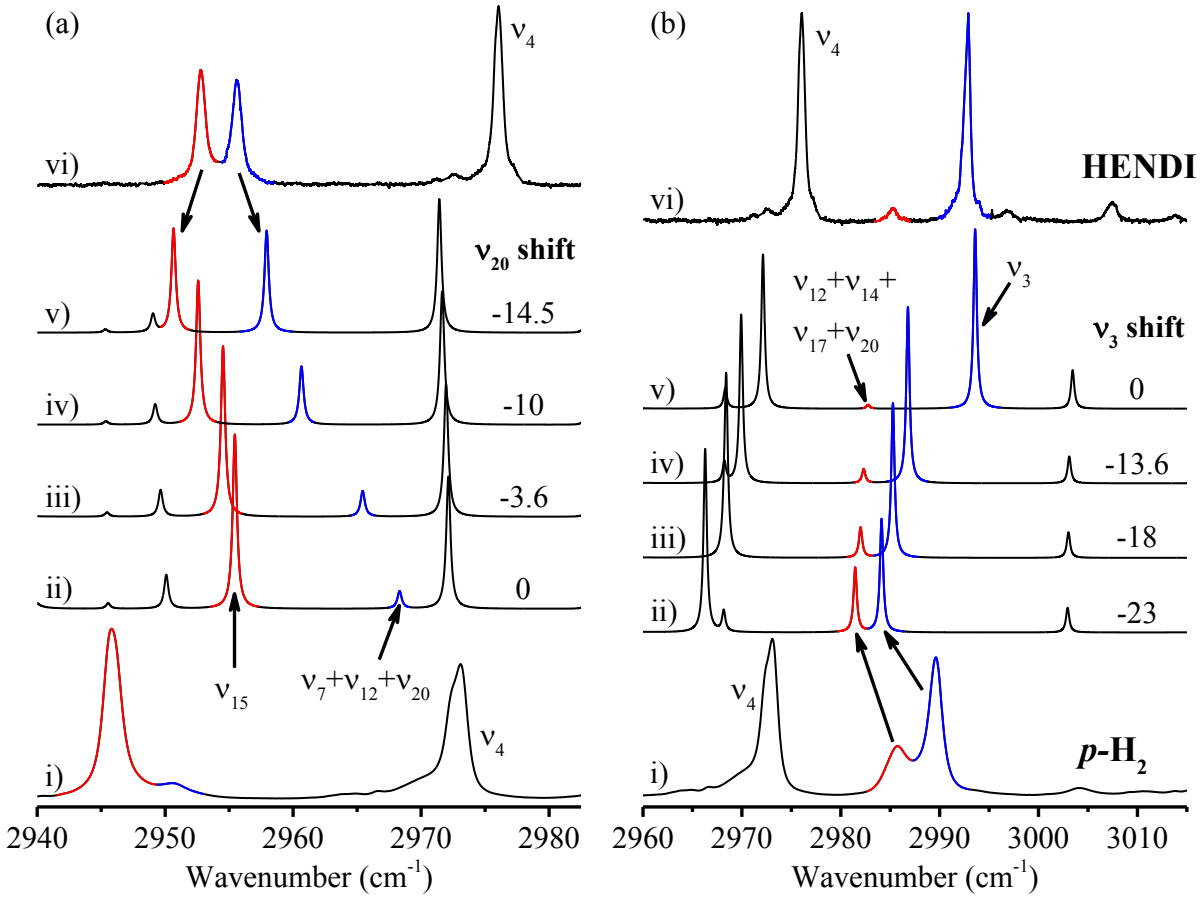

Fig. 2. The experimental spectra and the adjusted theoretical spectra for the regions 2940 – 2960 cm^{-1} and 2980 – 3000 cm^{-1}. (a)i) *p*-H_2 spectrum. (a)ii) Purely *ab initio* VPT2+K simulation. (a)iii) Theoretical spectrum that best reproduces the intensity ratio of the *p*-H_2 spectrum, with $\nu_7+\nu_{12}+\nu_{20}$ shifted by -3.6 cm^{-1}. (a)iv) Theoretical spectrum with $\nu_7+\nu_{12}+\nu_{20}$ shifted by -10 cm^{-1}. (a)v) Theoretical spectrum that best reproduces the intensity ratio of the HENDI spectrum, with $\nu_7+\nu_{12}+\nu_{20}$ shifted by -14.5 cm^{-1}. (a)vi) HENDI spectrum. (b)i) *p*-H_2 spectrum. (b)ii) Theoretical spectrum that best reproduces the intensity ratio of the *p*-H_2 spectrum, with ν_3 shifted by -23 cm^{-1}. (b)iii) Theoretical spectrum with ν_3 shifted by -18 cm^{-1}. (b)iv) Theoretical spectrum that best reproduces the intensity ratio of the HENDI spectrum, with ν_3 shifted by -13.6 cm^{-1}. (b)v) Purely *ab initio* VPT2+K simulation. (b)vi) HENDI spectrum.

Table 5. Relative intensity ratios and splittings of bands in experimental and theoretical spectra in the regions 2940 – 2960 cm^{-1} and 2980 – 3000 cm^{-1}.

Lower (2940 – 2960 cm^{-1})		
	Intensity Ratio	Splitting
Original VPT2+K	~91/9	12.9 cm^{-1}
p-H_2	~87/13	4.8 cm^{-1}
ν_{20}: -3.6 VPT2+K	~87/13	10.9 cm^{-1}
HENDI	~51/49	2.8 cm^{-1}
ν_{20}: -14.5 VPT2+K	~50/50	7.3 cm^{-1}

Upper (2980 – 3000 cm^{-1})		
	Intensity Ratio	Splitting
Original VPT2+K	~2/98	10.8 cm^{-1}
HENDI	~7/93	7.5 cm^{-1}
ν_3: -13.6 VPT2+K	~7/93	4.5 cm^{-1}
p-H_2	~36/64	3.9 cm^{-1}
ν_3: -23 VPT2+K	~36/64	2.7 cm^{-1}

In the *ab initio* VPT2+K Hamiltonian, the two states within each of the lower (ν_{15} / $\nu_7+\nu_{12}+\nu_{20}$) and upper (ν_3 / $\nu_{12}+\nu_{14}+\nu_{17}+\nu_{20}$) regions are not *directly* coupled, owing to the absence of ϕ_{ijkl} and ϕ_{ijklm} type force constants. Small portions of the effective Hamiltonian are extracted to highlight the origin of the *indirect* couplings, with the extracted Hamiltonian for the lower region given by

$$\widehat{\boldsymbol{H}}_{eff}^{lower} = \begin{array}{c} \begin{matrix} |\nu_{15}\rangle & |\nu_7+\nu_{16}\rangle & |\nu_7+\nu_{12}+\nu_{20}\rangle \end{matrix} \\ \begin{pmatrix} \nu_{15}^* & & \\ \frac{1}{2\sqrt{2}}\phi_{15,7,16} & (\nu_7+\nu_{16})^* & \\ \sim 0 & \frac{1}{2\sqrt{2}}\phi_{16,12,20} & (\nu_7+\nu_{12}+\nu_{20})^* \end{pmatrix} \end{array}, \quad (1)$$

and the extracted Hamiltonian for the upper region given by

$$\widehat{\boldsymbol{H}}_{eff}^{upper} = \begin{array}{c} \begin{matrix} |\nu_3\rangle & |\nu_7+\nu_8\rangle & |\nu_7+\nu_{12}+\nu_{14}\rangle & |\nu_{12}+\nu_{14}+\nu_{17}+\nu_{20}\rangle \end{matrix} \\ \begin{pmatrix} \nu_3^* & & & \\ \frac{1}{2\sqrt{2}}\phi_{3,7,8} & (\nu_7+\nu_8)^* & & \\ \sim 0 & \frac{1}{2\sqrt{2}}\phi_{8,12,14} & (\nu_7+\nu_{12}+\nu_{14})^* & \\ \sim 0 & \sim 0 & \frac{1}{2\sqrt{2}}\phi_{7,17,20} & (\nu_{12}+\nu_{14}+\nu_{17}+\nu_{20})^* \end{pmatrix} \end{array}. \quad (2)$$

The indirect couplings between the lower and upper states are ascertained by visual inspection of the entire effective Hamiltonian and determination of the coupling pathway involving the fewest possible intermediary states and the largest off-diagonal coupling terms. In the lower region, the lower state ν_{15} is coupled to the upper state $\nu_7+\nu_{12}+\nu_{20}$ through the intermediary state $\nu_7+\nu_{16}$. In the upper region, the lower state $\nu_{12}+\nu_{14}+\nu_{17}+\nu_{20}$ is coupled to the upper state ν_3 through two intermediary states. Specifically, $\nu_{12}+\nu_{14}+\nu_{17}+\nu_{20}$ is coupled to $\nu_7+\nu_{12}+\nu_{14}$, which is coupled to $\nu_7+\nu_8$, which is coupled to ν_3. The coupling "pathways" therefore consist of either two or three linked Fermi Resonances of type ν_i /$\nu_j+\nu_k$. The indirectness of the couplings points to the approximate nature of the two-state interaction models described above, for which single off-diagonal matrix elements are used to model entire coupling pathways. Nevertheless, the current analysis suggests that a comparison of *p*-H_2 and gas-phase spectra should be treated with caution for systems and spectral regions in which anharmonic resonance polyads are expected to be important, such as the CH stretching region. This may also be true for He droplets, although a definitive answer with respect to propene awaits a gas-phase jet-cooled spectrum in the 2940-3010 cm^{-1} region.

5. Summary

The infrared spectrum of propene in the CH stretching region was measured in both superfluid helium nanodroplets and a solid *para*-hydrogen matrix, to assess the differential matrix shifts associated with each host environment. Propene is an ideal molecule for testing these host environment effects, due to its highly anharmonic CH stretching region, which causes small matrix-induced perturbations of states to manifest as large changes in the relative intensities of bands in the experimental spectra. In the limit of 3N-6 uncoupled harmonic oscillators, 6 CH stretching vibrations are predicted for propene, and these mode descriptions

have been used to assign high-temperature gas-phase absorption spectra. However, the number of bands observed in the experimental He droplet and *p*-H_2 spectra is ~30, indicating that the harmonic approximation is not adequate for describing the CH stretch region for propene. We have used an anharmonic treatment to arrive at 14 band assignments, 7 of which have not been reported previously. The anharmonic model used here was the VPT2+K approach, which treats Fermi and Darling-Dennison resonances explicitly *via* the diagonalization of an effective Hamiltonian matrix. The Hamiltonian matrix contains deperturbed diagonal elements and off-diagonal coupling terms derived from a hybrid, semi-diagonal quartic force field computed at the CCSD(T)/ANO2//CCSD(T)/ANO1 level of theory. Two regions of the spectrum exhibit qualitatively different behavior, depending on the host environment. Simple two-state interaction models were employed to assess the differential matrix shifts that would be required to either tune or detune the associated resonances. We find that differential matrix shifts less than 10 cm^{-1} are sufficient to qualitatively affect the relative intensities observed in the propene CH stretching region.

Acknowledgements

We acknowledge support from the National Science Foundation (CHE-1664637). This work was supported by Ministry of Science and Technology, Taiwan (grant No. MOST106-2745-M009-001-ASP and MOST107-3017-F009-003) and the Center for Emergent Functional Matter Science of National Chiao Tung University from The Featured Areas Research Center Program within the framework of the Higher Education SPROUT Project by the Ministry of Education (MOE) in Taiwan.

References

[1] W.M. Coleman, B.M. Gordon, Examination of the matrix isolation fourier transform infrared spectra of organic compounds, part I, Appl. Spectrosc. 41 (1987) 886-889.

[2] S. Jagannathan, J.R. Cooper, C.L. Wilkins, Matrix effects in matrix isolation infrared spectroscopy, Appl. Spectrosc. 43 (1989) 781-786.

[3] M.E. Jacox, Comparison of the Ground-State Vibrational Fundamentals of Diatomic-Molecules in the Gas-Phase and in Inert Solid Matrices, J. Mol. Spectrosc. 113 (1985) 286-301.

[4] M.E. Jacox, The Vibrational-Energy Levels of Small Transient Molecules Isolated in Neon and Argon Matrices, Chem. Phys. 189 (1994) 149-170.

[5] M.C. Chan, M. Okumura, C.M. Gabrys, L.W. Xu, B.D. Rehfuss, T. Oka, High-resolution infrared spectroscopy of solid hydrogen, Phys. Rev. Lett. 66 (1991) 2060-2063.

[6] Y.P. Lee, Spectral and kinetic studies of free radicals of atmospheric interest, J. Chin. Chem. Soc. 39 (1992) 503-509.

[7] T. Oka, High-resolution spectroscopy of solid hydrogen, Annu. Rev. Phys. Chem. 44 (1993) 299-333.

[8] T. Momose, T. Shida, Matrix-isolation spectroscopy using solid parahydrogen as the matrix: Application to high-resolution spectroscopy, photochemistry, and cryochemistry, Bull. Chem. Soc. Jpn. 71 (1998) 1-15.

[9] T. Momose, H. Hoshina, M. Fushitani, H. Katsuki, High-resolution spectroscopy and the analysis of ro-vibrational transitions of molecules in solid parahydrogen, Vib. Spectrosc 34 (2004) 95-108.

[10] Y.P. Lee, Preparation and spectral characterization of novel species in matrices, J. Chin. Chem. Soc. 52 (2005) 641-650.

[11] T. Momose, M. Fushitani, H. Hoshina, Chemical reactions in quantum crystals, Int. Rev. Phys. Chem. 24 (2005) 533-552.

[12] K. Yoshioka, P.L. Raston, D.T. Anderson, Infrared spectroscopy of chemically doped solid parahydrogen, Int. Rev. Phys. Chem. 25 (2006) 469-496.

[13] M. Bahou, C.W. Huang, Y.L. Huang, J. Glatthaar, Y.P. Lee, Advances in use of *p*-H_2 as a novel host for matrix IR spectroscopy, J. Chin. Chem. Soc. 57 (2010) 771-782.

[14] M.E. Fajardo, Matrix isolation spectroscopy in solid parahydrogen: A primer, in: L. Khriachtchev (Ed.), Physics and Chemistry at Low Temperatures, Pan Stanford Publishing Pte Ltd, Singapore, 2011, pp. 167-202.

[15] J.P. Toennies, A.F. Vilesov, Spectroscopy of atoms and molecules in liquid helium, Annu. Rev. Phys. Chem. 49 (1998) 1-41.

[16] J.A. Northby, Experimental studies of helium droplets, J. Chem. Phys. 115 (2001) 10065-10077.

[17] J.P. Toennies, A.F. Vilesov, K.B. Whaley, Superfluid helium droplets: An ultracold nanolaboratory, Phys. Today 54 (2001) 31-37.

[18] J.P. Toennies, A.F. Vilesov, Superfluid helium droplets: A uniquely cold nanomatrix for molecules and molecular complexes, Angewandte Chemie-International Edition 43 (2004) 2622-2648.

[19] M.Y. Choi, G.E. Douberly, T.M. Falconer, W.K. Lewis, C.M. Lindsay, J.M. Merritt, P.L. Stiles, R.E. Miller, Infrared spectroscopy of helium nanodroplets: Novel methods for physics and chemistry, Int. Rev. Phys. Chem. 25 (2006) 15-75.

[20] F. Stienkemeier, K.K. Lehmann, Spectroscopy and dynamics in helium nanodroplets, Journal of Physics B-Atomic Molecular and Optical Physics 39 (2006) R127-R166.

[21] K. Kuyanov-Prozument, D. Skvortsov, M.N. Slipchenko, B.G. Sartakov, A. Vilesov, Matrix isolation spectroscopy in helium droplets, in: L. Khriachtchev (Ed.), Physics and Chemistry at Low Temperatures, Pan Stanford Publishing Pte Ltd, Singapore, 2011, pp. 203-230.

[22] S.F. Yang, A.M. Ellis, Helium droplets: A chemistry perspective, Chem. Soc. Rev. 42 (2013) 472-484.

[23] C.M. Lindsay, M.E. Fajardo, Infrared spectroscopy of hydrogen cyanide in solid parahydrogen, International Symposium on Molecular Spectroscopy, The Ohio State University, The Ohio State University, 2006.

[24] K. Nauta, R.E. Miller, Stark spectroscopy of polar molecules solvated in liquid helium droplets, Phys. Rev. Lett. 82 (1999) 4480-4483.

[25] D.T. Anderson, J.A. Hoag, Infrared spectroscopy of OCS isolated in solid parahydrogen, International Symposium on Molecular Spectroscopy, The Ohio State University, The Ohio State University, 2004.

[26] S. Grebenev, M. Hartmann, M. Havenith, B. Sartakov, J.P. Toennies, A.F. Vilesov, The rotational spectrum of single OCS molecules in liquid ^{4}He droplets, J. Chem. Phys. 112 (2000) 4485-4495.

[27] H. Katsuki, T. Momose, T. Shida, SF_6 and its clusters in solid parahydrogen studied by infrared spectroscopy, J. Chem. Phys. 116 (2002) 8411-8417.

[28] J. Harms, M. Hartmann, J.P. Toennies, A.F. Vilesov, B. Sartakov, Rotational structure of the IR spectra of single SF_6 molecules in liquid ^{4}He and ^{3}He droplets, J. Mol. Spectrosc. 185 (1997) 204-206.

[29] M.E. Fajardo, S. Tam, M.E. DeRose, Matrix isolation spectroscopy of H_2O, D_2O, and HDO in solid parahydrogen, J. Mol. Struct. 695 (2004) 111-127.

[30] K.E. Kuyanov, M.N. Slipchenko, A.F. Vilesov, Spectra of the ν_1 and ν_3 bands of water molecules in helium droplets, Chem. Phys. Lett. 427 (2006) 5-9.

[31] R. Schwan, M. Kaufmann, D. Leicht, G. Schwaab, M. Havenith, Infrared spectroscopy of the ν_2 band of the water monomer and small water clusters $(H_2O)_{n=2,3,4}$ in helium droplets, PCCP 18 (2016) 24063-24069.

[32] D.R. Lide, D.E. Mann, Microwave spectra of molecules exhibiting internal rotation .I. Propylene, J. Chem. Phys. 27 (1957) 868-873.

[33] D.R. Lide, D. Christensen, Molecular structure of propylene, J. Chem. Phys. 35 (1961) 1374-1378.

[34] G. Wlodarczak, J. Demaison, N. Heineking, A.G. Csaszar, The rotational spectrum of propene: Internal rotation analysis and *ab initio* and experimental centrifugal distortion constants, J. Mol. Spectrosc. 167 (1994) 239-247.

[35] N.C. Craig, P. Groner, A.R. Conrad, R. Gurusinghe, M.J. Tubergen, Microwave spectra for the three $^{13}C_1$ isotopologues of propene and new rotational constants for propene and its $^{13}C_1$ isotopologues, J. Mol. Spectrosc. 328 (2016) 1-6.

[36] L.J. Saethre, O. Svaeren, S. Svensson, S. Osborne, T.D. Thomas, J. Jauhiainen, S. Aksela, High-resolution C 1*s* photoelectron spectra of methane, ethene, propene, and 2-methylpropene, Phys. Rev. A 55 (1997) 2748-2756.

[37] R.C. Lord, P. Venkateswarlu, The infrared spectra of propylene and propylene-d_6, J. Opt. Soc. Am. 43 (1953) 1079-1085.

[38] B. Silvi, P. Labarbe, J.P. Perchard, Vibrational spectra and normal coordinates of four isotopes of propene, Spectrochimica Acta Part A-Molecular and Biomolecular Spectroscopy 29 (1973) 263-276.

[39] D.C. McKean, CH stretching frequencies, bond lengths and strengths in acetone, acetaldehyde, propene and isobutene, Spectrochimica Acta Part A-Molecular and Biomolecular Spectroscopy 31 (1975) 861-870.

[40] H.L. Fang, R.L. Swofford, M. McDevitt, A.B. Anderson, C-H stretching overtone spectrum of propylene. Molecular-orbital analysis in the local-mode model, J. Phys. Chem. 89 (1985) 225-229.

[41] J.R. Durig, G.A. Guirgis, S. Bell, Torsional spectrum and ab initio calculations for propene, J. Phys. Chem. 93 (1989) 3487-3491.

[42] L.C. Baylor, E. Weitz, Overtone spectroscopy of *cis*-propene-*1*,*2*-d_2, J. Phys. Chem. 94 (1990) 6209-6220.

[43] A. Ainetschian, G.T. Fraser, J. Ortigoso, B.H. Pate, Contaminated torsional tunneling splittings in five normal-mode vibrations of propene, J. Chem. Phys. 100 (1994) 729-732.

[44] O. Zakharieva, H. Forster, M. Turneva, Normal coordinate analysis of deutero propenes in the free and zeolite-adsorbed state, Spectrochimica Acta Part A-Molecular and Biomolecular Spectroscopy 50 (1994) 19-28.

[45] W.J. Lafferty, J.M. Flaud, M. Herman, Resolved torsional splitting in the ν_{18} and ν_{19}- bands of propene, J. Mol. Struct. 780-81 (2006) 65-69.

[46] E.T. Es-sebbar, M. Alrefae, A. Farooq, Infrared cross-sections and integrated band intensities of propylene: Temperature-dependent studies, J. Quant. Spectros. Radiat. Transfer 133 (2014) 559-569.

[47] E.M. Buzan, R.J. Hargreaves, P.F. Bernath, High resolution absorption cross sections for propylene in the 3 μm region at high temperatures, Molecular Astrophysics 3-4 (2016) 16-20.

[48] K. Sung, G.C. Toon, B.J. Drouin, A.W. Mantz, M.A.H. Smith, FT-IR measurements of cold propene (C_3H_6) cross-sections at temperatures between 150 and 299 K, J. Quant. Spectros. Radiat. Transfer 213 (2018) 119-132.

[49] P. Jona, M. Gussoni, G. Zerbi, Transferability of infrared intensity parameters. Application to propylene, J. Mol. Struct. 95 (1982) 15-21.

[50] M. Chhiba, G. Vergoten, The structures and vibrational frequencies of a series of linear alkenes obtained using the spectroscopic potential SPASIBA, J. Mol. Struct. 326 (1994) 35-58.

[51] J. Demaison, H.D. Rudolph, Ab initio anharmonic force field and equilibrium structure of propene, J. Mol. Spectrosc. 248 (2008) 66-76.

[52] K.M. Hickson, V. Wakelam, J.C. Loison, Methylacetylene (CH_3CCH) and propene (C_3H_6) formation in cold dense clouds: A case of dust grain chemistry, Molecular Astrophysics 3-4 (2016) 1-9.

[53] P.R. Franke, G.E. Douberly, Rotamers of isoprene: Infrared spectroscopy in helium droplets and ab initio thermochemistry, J. Phys. Chem. A 122 (2018) 148-158.

[54] C. Callegari, K.K. Lehmann, R. Schmied, G. Scoles, Helium nanodroplet isolation rovibrational spectroscopy: Methods and recent results, J. Chem. Phys. 115 (2001) 10090-10110.

[55] A.M. Morrison, T. Liang, G.E. Douberly, Automation of an "Aculight" continuous-wave optical parametric oscillator, Rev. Sci. Instrum. 84 (2013) 013102.

[56] A. Scheidemann, B. Schilling, J.P. Toennies, Anomalies in the reactions of He^+ with SF_6 embedded in large helium-4 clusters, J. Phys. Chem. 97 (1993) 2128-2138.

[57] M. Ovchinnikov, B.L. Grigorenko, K.C. Janda, V.A. Apkarian, Charge localization and fragmentation dynamics of ionized helium clusters, J. Chem. Phys. 108 (1998) 9351-9361.

[58] Y.P. Lee, Y.J. Wu, R.M. Lees, L.H. Xu, J.T. Hougen, Internal rotation and spin conversion of CH_3OH in solid para-hydrogen, Science 311 (2006) 365-368.

[59] Y.P. Lee, Y.J. Wu, J.T. Hougen, Direct spectral evidence of single-axis rotation and *ortho*-hydrogen-assisted nuclear spin conversion of CH_3F in solid *para*-hydrogen, J. Chem. Phys. 129 (2008) 104502.

[60] C.W. Huang, Y.C. Lee, Y.P. Lee, Diminished cage effect in solid *p*-H_2: Infrared spectra of ClSCS, ClCS, and ClSC in an irradiated *p*-H_2 matrix containing Cl_2 and CS_2, J. Chem. Phys. 132 (2010) 164303.

[61] P.R. Franke, D.P. Tabor, C.P. Moradi, G.E. Douberly, J. Agarwal, H.F. Schaefer, E.L. Sibert, Infrared laser spectroscopy of the *n*-propyl and *i*-propyl radicals: Stretch-bend Fermi coupling in the alkyl CH stretch region, J. Chem. Phys. 145 (2016) 224304.

[62] A.R. Brown, P.R. Franke, G.E. Douberly, Helium nanodroplet isolation of the cyclobutyl, 1-methylallyl, and allylcarbinyl radicals: Infrared spectroscopy and ab initio computations, J. Phys. Chem. A 121 (2017) 7576-7587.

[63] CFOUR, a quantum chemical program package written by J.F. Stanton, J. Gauss, M.E. Harding, P.G. Szalay with contributions from A.A. Auer, R.J. Bartlett, U. Benedikt, C. Berger, D.E. Bernholdt, Y.J. Bomble, L. Cheng, O. Christiansen, M. Heckert, O. Heun, C. Huber, T.-C. Jagau, D. Jonsson, J. Jusélius, K. Klein, W.J. Lauderdale, D.A. Matthews, T. Metzroth, L.A. Mück, D.P. O'Neill, D.R. Price, E. Prochnow, C. Puzzarini, K. Ruud, F. Schiffmann, W. Schwalbach, C. Simmons, S. Stopkowicz, A. Tajti, J. Vázquez, F. Wang, J.D. Watts and the integral packages MOLECULE (J. Almlöf and P.R. Taylor), PROPS (P.R. Taylor), ABACUS (T. Helgaker, H.J. Aa. Jensen, P. Jørgensen, and J. Olsen), and ECP routines by A. V. Mitin and C. van Wüllen. For the current version, see http://www.cfour.de.

[64] K. Raghavachari, G.W. Trucks, J.A. Pople, M. Head-Gordon, A fifth-order perturbation comparison of electron correlation theories, Chem. Phys. Lett. 157 (1989) 479-483.

[65] C. Hampel, K.A. Peterson, H.J. Werner, A comparison of the efficiency and accuracy of the quadratic configuration interaction (QCISD), coupled cluster (CCSD), and Brueckner coupled cluster (BCCD) methods, Chem. Phys. Lett. 190 (1992) 1-12.

[66] J.D. Watts, J. Gauss, R.J. Bartlett, Open-shell analytical energy gradients for triple excitation many-body, coupled-cluster methods: MBPT(4), CCSD+T(CCSD), CCSD(T), and QCISD(T), Chem. Phys. Lett. 200 (1992) 1-7.

[67] J.D. Watts, J. Gauss, R.J. Bartlett, Coupled-cluster methods with noniterative triple excitations for restricted open-shell Hartree-Fock and other general single determinant reference functions. Energies and analytical gradients, J. Chem. Phys. 98 (1993) 8718-8733.

[68] M.J.O. Deegan, P.J. Knowles, Perturbative corrections to account for triple excitations in closed and open shell coupled cluster theories, Chem. Phys. Lett. 227 (1994) 321-326.

[69] J.F. Stanton, Why CCSD(T) works: A different perspective, Chem. Phys. Lett. 281 (1997) 130-134.

[70] J. Almlof, P.R. Taylor, General contraction of Gaussian basis sets. I. Atomic natural orbitals for first- and second-row atoms, J. Chem. Phys. 86 (1987) 4070-4077.

[71] A.M. Rosnik, W.F. Polik, VPT2+K spectroscopic constants and matrix elements of the transformed vibrational Hamiltonian of a polyatomic molecule with resonances using Van Vleck perturbation theory, Mol. Phys. 112 (2014) 261-300.

[72] H.H. Nielsen, The vibration-rotation energies of molecules, Rev. Mod. Phys. 23 (1951) 90-136.

[73] D.A. Clabo, W.D. Allen, R.B. Remington, Y. Yamaguchi, H.F. Schaefer, A systematic study of molecular vibrational anharmonicity and vibration-rotation interaction by self-

consistent-field higher-derivative methods. Asymmetric top molecules, Chem. Phys. 123 (1988) 187-239.

[74] D.A. Matthews, J. Vazquez, J.F. Stanton, Calculated stretching overtone levels and Darling-Dennison resonances in water: A triumph of simple theoretical approaches, Mol. Phys. 105 (2007) 2659-2666.

[75] Mathematica, Version 10, Wolfram Research, Inc., Champaign, IL, 2016.

[76] J.M.L. Martin, T.J. Lee, P.R. Taylor, J.P. Francois, The anharmonic force field of ethylene, C_2H_4, by means of accurate *ab initio* calculations, J. Chem. Phys. 103 (1995) 2589-2602.

Supporting Information

Infrared Spectroscopy of Propene in Solid para-Hydrogen and Helium Droplets: the Role of Matrix Shifts in the Analysis of Anharmonic Resonances

Gregory T. Pullen[a], Peter R. Franke[a], Yuan-Pern Lee[b,c,d], and Gary E. Douberly[a]*

[a] Department of Chemistry, University of Georgia, Athens, GA 30602, USA

[b] Department of Applied Chemistry and Institute of Molecular Science, National Chiao Tung University, Hsinchu 30010, Taiwan

[c] Center for Emergent Functional Matter Science, National Chiao Tung University, Hsinchu 30010, Taiwan

[d] Institute of Atomic and Molecular Sciences, Academia Sinica, Taipei 10617, Taiwan

* Corresponding Author: Email: douberly@uga.edu Tele: 01-706-542-3857

Table S1. (see Table S1.csv)

Table S2. DVPT2 Harmonic and anharmonic frequencies and intensities in the region 2800 – 3120 cm^{-1}. The large anharmonic intensities (greater than 20 km/mol) are a consequence of some unidentified 1-1 and 1-2 resonant terms in the transition moments. However, the anharmonic transition moment expressions are not used to obtain the VPT2+K intensities or in any other subsequent calculations in this work.

	Harmonic Frequency (cm^{-1})	Harmonic Intensity (km/mol)	Anharm Frequency (cm^{-1})	Anharm Intensity (km/mol)
$2\nu_8$	2903.56	0	2824.37	0.12
$\nu_7+\nu_9$	2904.15	0	2828.20	0.23
$\nu_7+\nu_{16}$	2982.67	0	2845.20	0.41
$\nu_7+\nu_8$	2949.82	0	2866.05	1.18
$2\nu_7$	2996.09	0	2911.15	10.74
ν_5	3030.82	19.59	2914.87	7.65
$\nu_6+\nu_{10}$	3015.46	0	2926.17	0.41
ν_{15}	3093.55	16.79	2948.06	18.36
ν_4	3117.29	10.98	2969.67	14.30
ν_3	3141.55	13.62	3003.45	2088.87
$\nu_6+\nu_9$	3101.08	0	3019.75	5.33
ν_2	3155.77	11.49	3036.16	85.87
$\nu_6+\nu_8$	3146.75	0	3046.96	317.88
ν_1	3233.95	14.35	3088.34	17.15
$\nu_6+\nu_7$	3193.01	0	3111.56	0.58

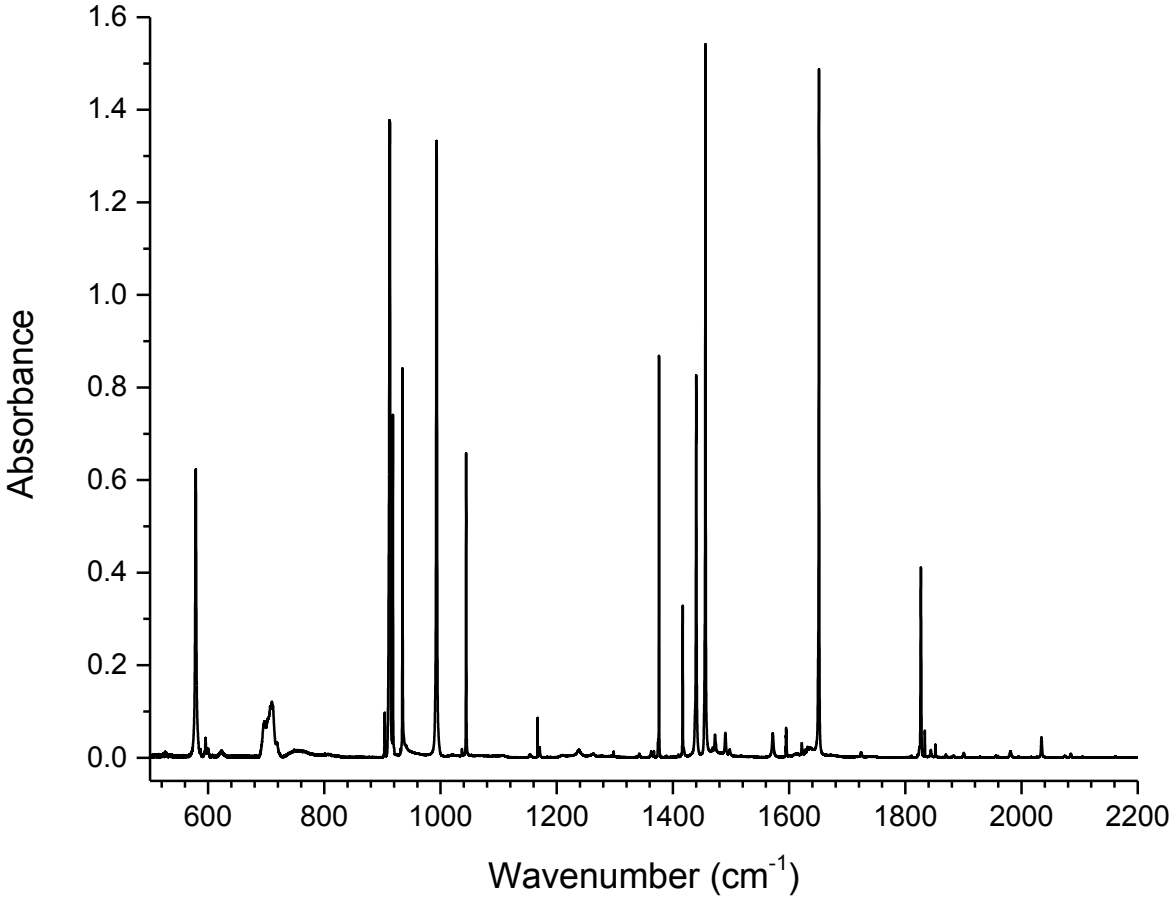

Fig. S1. *p*-H_2 spectrum from 500 – 2200 cm^{-1}.

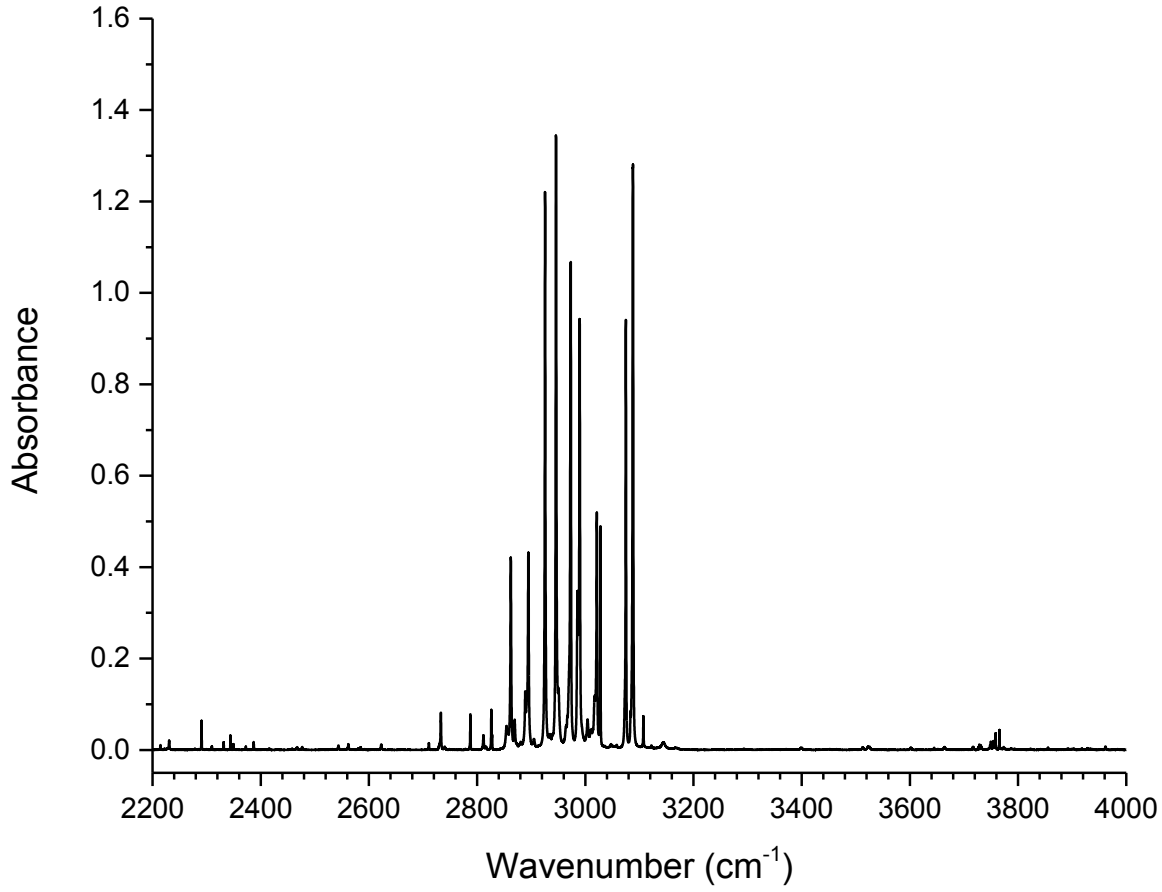

Fig. S2. *p*-H_2 spectrum from 2200 – 4000 cm^{-1}.

Table S3. Assignments for the *p*-H_2 and HENDI spectra, with comparisons to previous literature.

	This Work			Silvi,	Ainetschian,	Lafferty,	Es-sebbar,
Assignment	***p*-H_2**	**HENDI**	**VPT2+K**	**et. al.**	**et. al. [1]**	**et. al. [2]**	**et. al. [3]**
ν_1	3087.98	3093.45	3091.5	3091			3091.62
ν_2	3021.3	3023.7	3022.5				
ν_3 / $\nu_{12}+\nu_{14}+\nu_{17}+\nu_{20}$	2985.74	2985.26	2982.8				
ν_3 / $\nu_{12}+\nu_{14}+\nu_{17}+\nu_{20}$	2989.61	2992.8	2993.6	2991			2991.03
ν_4	2972.8	2976	2972.1	2973			
ν_5	2925.61	2932	2939.2	2932			2931.46
ν_6	1651.3		1654.4	1653			1653.18
ν_7	1455.9		1460.1	1459			1451.04
ν_8	1416.9		1417.9	1414			
ν_9	1376		1377.6	1378			1377.94
ν_{10}	1298		1295.5	1298			1297.86
ν_{11}	1170.6		1169.3	1170			1170.04
ν_{12}	934.4		933	934.5	935.67		
ν_{13}	918		916.1	919	919.29		
ν_{14}			422	428			426.02
ν_{15} / $\nu_7+\nu_{12}+\nu_{20}$	2945.87	2952.8	2955.4	2953			2954.3
ν_{15} / $\nu_7+\nu_{12}+\nu_{20}$	2950.66	2955.6	2968.3				
ν_{16} / $\nu_{14}+\nu_{17}$	1440.1		1442.2	1443			1442.71
ν_{16} / $\nu_{14}+\nu_{17}$	1472.5		1470.7				
ν_{17}	1044		1043.6	1045	1045.2		1045.04
ν_{18}	993.1		992.1	990	990.78	990.7761	991.05
ν_{19}	912.5		910.9	912	912.67	912.6677	912.62
ν_{20}	578.7		574.2	575.2			576.27
ν_{21}			187.7	188			
$\nu_6+\nu_7$	3107.37	3113.2	3116.7				
$\nu_6+\nu_8$	3074.97	3079.4	3081.6				
$\nu_6+\nu_9$	3027.87	3033.14	3035.1				
$2\nu_7$				2892			
$\nu_6+\nu_{12}+\nu_{14}$	3004.15	3007.41	3003.5				
$\nu_{14}+\nu_{16}+\nu_{17}$	2894.7	2899.96	2896				
$2\nu_{16}$	2862.31	2867.8	2867.3	2868			
$\nu_{21}+\nu_{17}$			1227.8	1231			

Table S4. VPT2+K frequencies, intensities, and compositions in the region 2800 – 3120 cm^{-1}. Bands that have been confidently assigned in the experimental spectrum are marked with bold type. The largest contributing eigenvector components (which inform the assignments given in Fig. 1) are also shown in bold.

cm^{-1}	Int (km/mol)	Composition
2815.09	0.40	3% ν_{15} + 81% $\nu_9+\nu_{16}$ + 2% $\nu_9+\nu_{12}+\nu_{20}$ + 12% $\nu_9+\nu_{14}+\nu_{17}$ + 2% $\nu_{12}+\nu_{14}+\nu_{16}$
2817.46	0.16	1% ν_1 + 84% $\nu_6+\nu_{11}$ + 1% $\nu_7+\nu_9$ + 1% $\nu_7+\nu_{10}$ + 1% $2\nu_8$ + 11% $\nu_7+\nu_{12}+\nu_{14}$ + 1% $2\nu_{12}+2\nu_{14}$
2827.32	0.60	2% ν_2 + 2% ν_3 + 1% $\nu_6+\nu_{11}$ + 1% $\nu_7+\nu_8$ + 5% $\nu_7+\nu_9$ + 82% $2\nu_8$ + 1% $\nu_8+\nu_9$ + 2% $2\nu_9$ + 3% $\nu_8+\nu_{12}+\nu_{14}$
2832.92	0.34	2% ν_4 + 1% ν_5 + 1% $\nu_6+\nu_{11}$ + 1% $\nu_7+\nu_8$ + 86% $\nu_7+\nu_9$ + 4% $2\nu_8$ + 1% $\nu_8+\nu_9$ + 2% $2\nu_{16}$ + 1% $\nu_9+\nu_{12}+\nu_{14}$
2844.07	0.11	1% ν_{15} + 11% $\nu_9+\nu_{16}$ + 1% $\nu_7+\nu_{14}+\nu_{17}$ + 2% $\nu_8+\nu_{14}+\nu_{17}$ + 1% $\nu_9+\nu_{12}+\nu_{20}$ + 82% $\nu_9+\nu_{14}+\nu_{17}$ + 1% $\nu_{12}+\nu_{14}+\nu_{16}$ + 1% $\nu_{12}+2\nu_{14}+\nu_{17}$
2867.28	**3.95**	**21% ν_5** + 4% $2\nu_7$ + **19% $\nu_7+\nu_8$** + 1% $\nu_7+\nu_9$ + 4% $\nu_8+\nu_9$ + 6% $2\nu_9$ + **35% $2\nu_{16}$** + 1% $\nu_7+\nu_{12}+\nu_{14}$ + 1% $\nu_{12}+\nu_{16}+\nu_{20}$ + 6% $\nu_{14}+\nu_{16}+\nu_{17}$ + 1% $2\nu_{14}+2\nu_{17}$
2874.02	0.49	1% ν_3 + 3% ν_4 + 63% $\nu_7+\nu_8$ + 2% $\nu_7+\nu_9$ + 2% $2\nu_8$ + 19% $2\nu_{16}$ + 2% $\nu_7+\nu_{12}+\nu_{14}$ + 1% $\nu_8+\nu_{12}+\nu_{14}$ + 1% $\nu_{12}+\nu_{16}+\nu_{20}$ + 5% $\nu_{14}+\nu_{16}+\nu_{17}$
2887.49	0.19	1% ν_{15} + 3% $\nu_7+\nu_{16}$ + 7% $\nu_8+\nu_{16}$ + 1% $\nu_7+\nu_{14}+\nu_{17}$ + 1% $\nu_8+\nu_{12}+\nu_{20}$ + 54% $\nu_8+\nu_{14}+\nu_{17}$ + 27% $\nu_9+\nu_{12}+\nu_{20}$ + 1% $\nu_9+\nu_{14}+\nu_{17}$ + 1% $\nu_{12}+\nu_{14}+\nu_{16}$ + 1% $2\nu_{12}+\nu_{14}+\nu_{20}$ + 2% $\nu_{12}+2\nu_{14}+\nu_{17}$
2894.41	1.49	10% ν_{15} + 72% $\nu_7+\nu_{16}$ + 2% $\nu_9+\nu_{16}$ + 1% $\nu_7+\nu_{12}+\nu_{20}$ + 7% $\nu_7+\nu_{14}+\nu_{17}$ + 5% $\nu_9+\nu_{12}+\nu_{20}$ + 1% $\nu_9+\nu_{14}+\nu_{17}$ + 1% $\nu_{12}+\nu_{14}+\nu_{16}$
2896.00	**3.42**	**18% ν_5 + 19% $2\nu_7$** + 5% $\nu_7+\nu_8$ + 1% $2\nu_8$ + 2% $2\nu_9$ + 1% $2\nu_{16}$ + **40% $\nu_{14}+\nu_{16}+\nu_{17}$** + 1% $\nu_{12}+\nu_{14}+\nu_{17}+\nu_{20}$ + 11% $2\nu_{14}+2\nu_{17}$
2907.42	1.02	3% ν_4 + 4% ν_5 + 28% $2\nu_7$ + 2% $\nu_7+\nu_8$ + 22% $2\nu_{16}$ + 2% $\nu_{12}+\nu_{16}+\nu_{20}$ + 23% $\nu_{14}+\nu_{16}+\nu_{17}$ + 13% $2\nu_{14}+2\nu_{17}$
2926.11	0.54	4% ν_{15} + 3% $\nu_7+\nu_{16}$ + 1% $\nu_7+\nu_{12}+\nu_{20}$ + 68% $\nu_7+\nu_{14}+\nu_{17}$ + 21% $\nu_8+\nu_{12}+\nu_{20}$ + 1% $2\nu_{12}+\nu_{14}+\nu_{20}$ + 2% $\nu_{12}+2\nu_{14}+\nu_{17}$
2926.56	2.05	1% ν_1 + 13% ν_2 + 2% ν_3 + 3% ν_4 + 1% $\nu_6+\nu_8$ + 77% $\nu_6+\nu_{10}$ + 1% $\nu_8+\nu_{10}$ + 1% $2\nu_{10}$ + 1% $\nu_6+\nu_{12}+\nu_{14}$
2927.06	0.19	1% ν_{15} + 2% $\nu_7+\nu_{16}$ + 2% $\nu_8+\nu_{16}$ + 1% $\nu_7+\nu_{12}+\nu_{20}$ + 20% $\nu_7+\nu_{14}+\nu_{17}$ + 71% $\nu_8+\nu_{12}+\nu_{20}$ + 2% $2\nu_{12}+\nu_{14}+\nu_{20}$
2939.24	**5.55**	**29% ν_5** + **35% $2\nu_7$** + 1% $\nu_7+\nu_8$ + 1% $\nu_8+\nu_9$ + 2% $2\nu_9$ + 3% $2\nu_{16}$ + **16% $\nu_{12}+\nu_{16}+\nu_{20}$** + 1% $\nu_{14}+\nu_{16}+\nu_{17}$ + 1% $2\nu_{12}+2\nu_{20}$ + 2% $\nu_{12}+\nu_{14}+\nu_{17}+\nu_{20}$ + 10% $2\nu_{14}+2\nu_{17}$
2945.54	0.33	2% ν_5 + 2% $2\nu_7$ + 1% $2\nu_{16}$ + 9% $\nu_{12}+\nu_{16}+\nu_{20}$ + 22% $\nu_{14}+\nu_{16}+\nu_{17}$ + 1% $2\nu_{12}+2\nu_{20}$ + 63% $2\nu_{14}+2\nu_{17}$
2950.09	2.06	2% ν_4 + 10% ν_5 + 8% $2\nu_7$ + 1% $\nu_7+\nu_8$ + 9% $2\nu_{16}$ + 56% $\nu_{12}+\nu_{16}+\nu_{20}$ + 1% $\nu_{14}+\nu_{16}+\nu_{17}$ + 4% $2\nu_{12}+2\nu_{20}$ + 8% $\nu_{12}+\nu_{14}+\nu_{17}+\nu_{20}$ + 1% $2\nu_{14}+2\nu_{17}$
2955.44	**10.59**	**71% ν_{15}** + 12% $\nu_7+\nu_{16}$ + 2% $\nu_9+\nu_{16}$ + 1% $\nu_{11}+\nu_{16}$ + 12% $\nu_7+\nu_{12}+\nu_{20}$ + 1% $\nu_7+\nu_{14}+\nu_{17}$
2968.32	**1.06**	7% ν_{15} + 7% $\nu_7+\nu_{16}$ + **82% $\nu_7+\nu_{12}+\nu_{20}$** + 1% $\nu_8+\nu_{12}+\nu_{20}$ + 2% $2\nu_{12}+\nu_{14}+\nu_{20}$
2972.13	**8.03**	1% ν_2 + 16% ν_3 + **60% ν_4** + 4% $\nu_6+\nu_8$ + 4% $\nu_6+\nu_{10}$ + 1% $2\nu_7$ + 1% $\nu_7+\nu_9$ + 1% $2\nu_8$ + 1% $\nu_9+\nu_{11}$ + 4% $2\nu_{16}$ + 1% $\nu_6+\nu_{12}+\nu_{14}$ + 3% $\nu_{12}+\nu_{14}+\nu_{17}+\nu_{20}$
2982.78	**0.21**	1% ν_3 + 1% $2\nu_{16}$ + 7% $\nu_{12}+\nu_{16}+\nu_{20}$ + 3% $\nu_{14}+\nu_{16}+\nu_{17}$ + 2% $2\nu_{12}+2\nu_{20}$ + **85% $\nu_{12}+\nu_{14}+\nu_{17}+\nu_{20}$**

2993.59	**9.34**	**52% ν_3** + 21% ν_4 + 7% $\nu_6+\nu_8$ + 8% $\nu_6+\nu_9$ + 3% $\nu_7+\nu_8$ + 1% $2\nu_8$ + 2% $2\nu_{16}$ + 4% $\nu_6+\nu_{12}+\nu_{14}$
3003.45	**2.01**	12% ν_2 + 5% ν_3 + 1% $\nu_6+\nu_7$ + 1% $\nu_6+\nu_8$ + **79% $\nu_6+\nu_{12}+\nu_{14}$**
3022.46	**6.50**	**61% ν_2** + 1% $2\nu_6$ + 4% $\nu_6+\nu_8$ + 3% $\nu_6+\nu_9$ + 17% $\nu_6+\nu_{10}$ + 1% $2\nu_8$ + 1% $2\nu_{10}$ + 12% $\nu_6+\nu_{12}+\nu_{14}$
3035.06	**1.18**	2% ν_2 + 6% ν_3 + 1% ν_4 + 2% $\nu_6+\nu_8$ + **88% $\nu_6+\nu_9$**
3081.60	**3.58**	15% ν_1 + 4% ν_2 + 9% ν_3 + 3% $\nu_6+\nu_7$ + **67% $\nu_6+\nu_8$** + 1% $\nu_6+\nu_{12}+\nu_{14}$
3091.53	**10.87**	**81% ν_1** + 1% ν_2 + 2% ν_3 + 2% $\nu_6+\nu_7$ + 11% $\nu_6+\nu_8$ + 1% $\nu_6+\nu_{10}$ + 1% $\nu_6+\nu_{11}$
3116.72	**0.44**	3% ν_3 + **93% $\nu_6+\nu_7$** + 3% $\nu_6+\nu_8$ + 1% $\nu_6+\nu_{12}+\nu_{14}$

a)i) **Lower – HENDI**

$$\begin{pmatrix} \sqrt{0.505} & \sqrt{0.495} \\ -\sqrt{0.495} & \sqrt{0.505} \end{pmatrix} \begin{pmatrix} 2952.8 & 0 \\ 0 & 2955.6 \end{pmatrix} \begin{pmatrix} \sqrt{0.505} & \sqrt{0.495} \\ -\sqrt{0.495} & \sqrt{0.505} \end{pmatrix}^{-1} = \begin{pmatrix} 2954.19 & 1.40 \\ 1.40 & 2954.21 \end{pmatrix}$$

a)ii) **Lower – *p*-H_2**

$$\begin{pmatrix} \sqrt{0.869} & \sqrt{0.131} \\ -\sqrt{0.131} & \sqrt{0.869} \end{pmatrix} \begin{pmatrix} 2945.87 & 0 \\ 0 & 2950.66 \end{pmatrix} \begin{pmatrix} \sqrt{0.869} & \sqrt{0.131} \\ -\sqrt{0.131} & \sqrt{0.869} \end{pmatrix}^{-1} = \begin{pmatrix} 2946.50 & 1.62 \\ 1.62 & 2950.03 \end{pmatrix}$$

b)i) **Upper – HENDI**

$$\begin{pmatrix} \sqrt{0.926} & \sqrt{0.074} \\ -\sqrt{0.074} & \sqrt{0.926} \end{pmatrix} \begin{pmatrix} 2985.26 & 0 \\ 0 & 2992.8 \end{pmatrix} \begin{pmatrix} \sqrt{0.926} & \sqrt{0.074} \\ -\sqrt{0.074} & \sqrt{0.926} \end{pmatrix}^{-1} = \begin{pmatrix} 2985.82 & 1.98 \\ 1.98 & 2992.24 \end{pmatrix}$$

b)ii) **Upper – *p*-H_2**

$$\begin{pmatrix} \sqrt{0.643} & \sqrt{0.357} \\ -\sqrt{0.357} & \sqrt{0.643} \end{pmatrix} \begin{pmatrix} 2985.74 & 0 \\ 0 & 2989.61 \end{pmatrix} \begin{pmatrix} \sqrt{0.643} & \sqrt{0.357} \\ -\sqrt{0.357} & \sqrt{0.643} \end{pmatrix}^{-1} = \begin{pmatrix} 2987.12 & 1.85 \\ 1.85 & 2988.23 \end{pmatrix}$$

Equation S1. Experimentally determined initial states and off-diagonal coupling terms, assuming a two state interaction with a bright state and a dark state. a) Lower region from 2940 – 2960 cm^{-1}, for (i) the HENDI spectrum and (ii) the *p*-H_2 spectrum. b) Upper region from 2980 – 3000 cm^{-1}, for (i) the HENDI spectrum and (ii) the *p*-H_2 spectrum.

References

[1] A. Ainetschian, G.T. Fraser, J. Ortigoso, B.H. Pate, Contaminated torsional tunneling splittings in five normal-mode vibrations of propene, J. Chem. Phys. 100 (1994) 729-732.

[2] W.J. Lafferty, J.M. Flaud, M. Herman, Resolved torsional splitting in the ν_{18} and ν_{19}- bands of propene, J. Mol. Struct. 780-81 (2006) 65-69.

[3] E.T. Es-sebbar, M. Alrefae, A. Farooq, Infrared cross-sections and integrated band intensities of propylene: Temperature-dependent studies, J. Quant. Spectros. Radiat. Transfer 133 (2014) 559-569.